2019

Area-scalable high-heat-flux dissipation at low thermal resistance using a capillary-fed two-layer evaporator wick

S. Sudhakar
Purdue University

J. A. Weibel
Purdue University, jaweibel@purdue.edu

F. Zhou
Toyota

E. M. Dede
Toyota

S V. Garimella
Purdue University, sureshg@purdue.edu

Sudhakar, S.; Weibel, J. A.; Zhou, F.; Dede, E. M.; and Garimella, S V., "Area-scalable high-heat-flux dissipation at low thermal resistance using a capillary-fed two-layer evaporator wick" (2019). *CTRC Research Publications.* Paper 347.
http://dx.doi.org/doi.org/10.1016/j.ijheatmasstransfer.2019.02.075

Area-Scalable High-Heat-Flux Dissipation at Low Thermal Resistance Using a Capillary-Fed Two-layer Evaporator Wick[1]

Srivathsan Sudhakar[*], Justin A. Weibel[*2], Feng Zhou[**], Ercan M. Dede[**], Suresh V. Garimella[*]

[*]School of Mechanical Engineering
Purdue University, 585 Purdue Mall, West Lafayette, IN 47907 USA

[**]Electronics Research Department
Toyota Research Institute of North America, 1555 Woodridge Avenue, MI 48105 USA

Abstract

A two-layer sintered porous evaporator wick for use in vapor chambers is shown to offer very high performance in passive high-heat-flux dissipation over large areas at a low thermal resistance. The two-layer wick has an upper cap layer dedicated to capillary liquid feeding of a thin base layer below that supports boiling. An array of vertical posts bridges these two layers for liquid feeding, while vents in the cap layer provide an unimpeded pathway for vapor removal from the base wick. The two-layer wick is fabricated using a combination of sintering and laser machining processes. The thermal resistance of the wicks during boiling is characterized in a saturated environment that replicates the capillary-fed working conditions of a vapor chamber evaporator. Thermal characterization tests are first performed using conventional single-layer evaporator wicks to analyze the effect of sintered particle size on capillary-fed boiling of water. Of the particle size ranges tested, wicks sintered from 180-212 μm-diameter particles provided the best combination of high dryout heat flux and a low boiling resistance. A two-layer evaporator wick comprising particles of this optimal size and a 15 × 15 array of liquid feeding posts yielded a maximum heat flux dissipation of 485 W/cm^2 over a 1 cm^2 heat input area while also maintaining a low thermal resistance of only ~0.052 K/W. The thermal performance of the two-layer wick is compared against various hybrid and biporous evaporator wicks previously investigated in the literature. While previous wick designs are typically restricted to small areas and low power levels or high surface superheats when dissipating such heat fluxes, the unique area-scalability of the two-layer wick design allows it to achieve an unprecedented combination of high total power and low-thermal-resistance heat dissipation over larger areas than were previously possible.

---

[1] Submitted for possible publication in *International Journal of Heat and Mass Transfer*, 2018.

[2] Corresponding author, E-mail address: jaweibel@purdue.edu.

Keywords

High-heat-flux dissipation, low thermal resistance, capillary-fed boiling, sintered wick, vapor chamber, two-layer evaporator wick, dryout

Nomenclature

A	area (m^2)
d	diameter (m)
D	particle diameter (m)
K	permeability (m^2)
l	length (m)
P	pressure (Pa)
q	heat flux (W/m^2)
Q	heat input (W)
R	resistance (K/W)
t	thickness (m)

Greek symbols

φ	porosity (-)

Subscript

base	base wick
bulk	bulk wick
c	capillary
cap	cap layer
evap	evaporator
post	liquid-feeding post
vent	vapor vent

1 Introduction

The use of vapor chambers or flat heat pipes in thermal management applications is attractive due to their effective passive heat spreading capability and reliability [1-3]. Recently, there has been a focus on increasing the power dissipation limits of vapor chambers by improving the thermal-hydraulic performance of the porous wick at the location of heat input (*i.e.*, the evaporator), where high local heat fluxes may induce boiling in the wick [4,5]. In comparison to homogeneous or monoporous evaporator wicks, hybrid [6-9] and biporous [10-13] evaporator wick designs have successfully sustained higher heat fluxes by phase change during capillary feeding. The design rationale and performance tradeoffs reported in the literature, specifically for high-heat-flux dissipation during capillary-fed boiling from evaporator wicks, are reviewed in this section.

Recent developments related to porous evaporator wicks for capillary-fed boiling, all using water as the working fluid, are summarized in Table 1. This table chronologically catalogs the evaporator wick types, saturation temperature during testing, heater size, maximum heat flux, maximum total power dissipation, and the superheat and thermal resistance at the maximum power dissipation. Sintered copper porous wicks are most commonly used for capillary-fed boiling due to their high conductivity and because they offer many parallel fluid flow paths for liquid replenishment during boiling. Weibel *et al*. [14] studied evaporation and boiling behaviors from sintered monoporous copper wicks and reported heat flux dissipation greater than 500 W/cm^2. To improve on the thermal performance of monoporous wicks, different surface nanostructuring techniques and chemical modifications have been evaluated in the literature. In the case of copper wicks, growing copper oxide (CuO) nanostructures improves the wettability of the wick [15,16]. In addition to increasing the capillary performance, the roughness of the CuO nanostructures has been shown to provide increased nucleation site densities, which enhances the heat transfer coefficients during boiling. Nam *et al.* [15] showed that nanostructuring copper micro-post wicks enhances the dryout heat flux by 70% compared to bare copper micro-posts, reporting dryout heat fluxes as high as ~800 W/cm^2. Nevertheless, monoporous wicks have one characteristic pore size, which can be tuned to either provide a high capillary pressure or high permeability, but not a combination of both. Biporous wicks overcome this limitation, where the larger pores offer a high permeability for better liquid feeding, while the smaller pores can sustain liquid menisci for capillary feeding during high-heat-flux operation. Biporous wicks composed of patterned carbon nanotube (CNT) forests were investigated by Cai and Chen [11] and shown to dissipate extreme heat fluxes of ~900 W/cm^2; Semenic and Catton [10] used sintered copper biporous wicks to dissipate 990 W/cm^2.

While extremely high heat fluxes have been passively dissipated by capillary-fed boiling, Table 1 reveals that these fluxes are either limited to small hotspots (typically less than a few mm^2 and ~10s of W total power) or are attained at a very large surface superheat above the saturation temperature. Multiple studies have clearly demonstrated that there is a very strong inverse relationship between the heat input area and the dryout heat flux that can be supported by capillary-fed boiling. For example, Coso and Srinivasan [12] observed (for their biporous silicon pin fin wicks) that the maximum heat flux decreased from 733 W/cm^2 to 277 W/cm^2 when the heat input area was increased from 6.25 mm^2 (2.5 mm × 2.5 mm) to 100 mm^2 (10 mm × 10 mm). This effect can be primarily attributed to the increased fluid flow length to feed liquid to the center of the larger heated areas. Very thick wicks, on the other hand, can sustain high heat fluxes over somewhat larger areas, but the added impedance, posed by the longer vapor travel paths from the substrate through the thicker wick, induce a high surface superheat in this case. For example, the 990 W/cm^2 of heat flux dissipated using sintered copper biporous wicks over 32 mm^2 [10] was attained at a surface superheat of ~150 K.

Effective fluid delivery throughout the evaporator region and efficient vapor removal from the wick are both necessary to enhance the dryout limits of porous wicks over larger evaporator areas (~1 cm^2). A few different hybrid sintered evaporator wick designs have been proposed to achieve this goal. Dai *et al*. [8] used a combination of sintered screen mesh and rectangular microchannels for the evaporator wick; the microchannels provide high-permeability pathways for liquid feeding, while the smaller pores in the screen mesh provide a high capillary pressure. These wicks demonstrated 150 W/cm^2 dissipated over an area of 1 cm^2. Hwang *et al*. [6] fabricated and tested a sintered copper evaporator wick with lateral converging arteries that feed a thin layer of sintered particles within the heated area. The arteries provide liquid feeding while the small thickness of the sintered layer keeps its thermal resistance to a minimum. Heat fluxes of ~580 W/cm^2 were dissipated over a 1 cm^2 heater area, albeit at a high superheat of ~72 K. The high superheat was attributed to local dryout occurring in the center of the heated area.

In our previous work, we designed a two-layer evaporator wick [17] to achieve high heat flux dissipation over large heater areas at a low thermal resistance. The two-layer evaporator wick, as shown in Figure 1 (a), comprises a thin base wick to support low-resistance boiling, that is supplied with liquid through an array of vertical posts attached to a thick cap layer above. In addition, vapor vents in the cap layer allow for the vapor generated by boiling in the thin base wick layer to escape. Fabrication and testing of a prototype two-layer wick [18] confirmed this working mechanism during capillary-fed boiling. The two-layer wick decoupled liquid feeding from vapor removal, thus providing an unrestricted pathway for distributed liquid supply to the base wick, without the occurrence of any local dryout that would otherwise increase the superheat. In the current study, we demonstrate high-heat-flux dissipation using the two-layer evaporator wick previously introduced. The fabrication steps and the internal structure of the two-layer wick are first described, and the effect of sintered particle size on the capillary-fed boiling behavior is then studied for a benchmark single-layer wick. Subsequently, a two-layer wick composed of the best-performing particle size is characterized and its performance compared to the literature.

2 Characterization and imaging of the two-layer wick structure

The process steps involved in the fabrication of the two-layer evaporator wick were previously presented in Ref. [18]. To briefly review, a layer of copper particles is first sintered on a copper substrate, followed by subtractive laser machining to form the posts and expose a thin base wick layer over the center 1 cm^2 heater/evaporator area. This first layer is then inverted onto a second layer of loose copper particles and sintered together, which results in a cap layer that is connected to the top of the posts for liquid feeding to the base layer. The vapor vents are then laser-machined through the cap layer, offset from the posts. The structure of the two-layer wick is shown in Figure 1 (a) which identifies the key features.

While most of the prior hybrid evaporator wicks have been fabricated using copper particles sintered in a single step [6,7], the two-layer wick required two separate sintering processes. It is thus critical to confirm that sintering yielded connectivity between the layers of the wick, as required for the desired top-down liquid-feeding to function. In addition, it is important to ensure proper alignment between the layers and confirm that the vapor vents were offset from the posts. Furthermore, the effect of laser ablation on the morphology of the sintered copper wick is characterized to confirm that the primary liquid-feeding path was not impeded. Hence, this section briefly describes the laser machining parameters that were used for fabrication and investigates the internal structure of an as-fabricated two-layer wick through scanning electron microscopy (SEM) and micro-computed tomography (μ-CT) scanning. To destructively investigate the internal structure and surface characteristics resulting from this fabrication approach, an additional two-layer wick sample was fabricated with a 4 × 4 array of liquid feeding posts and an offset 3 × 3 array of vents.

The laser machining process is briefly described here and the laser parameters specified. A multi-wavelength fiber laser (Universal Laser Systems PLS6MW, Birck Nanotechnology Center, Purdue University) is used to ablate the sintered wick to form the features. In each pass across the surface, the laser ablates a portion of the material and achieves a depth on the order of tens of microns. Multiple passes of the laser are required to fabricate the posts and the vents in the two-layer wick having heights on the order of hundreds of microns. The laser power and raster speed can be controlled to affect the ablation depth during each pass. A fabrication recipe was developed by varying the laser power and speeds to identify a combination that gave a near-linear relationship between the ablation depth and number of passes. This recipe was tuned specifically to each sintered particle size and then employed to control the depth. The structure of a two-layer wick fabricated with 90-106 μm particles and a combination of 70% laser power and 10% raster speed is presented below.

2.1 SEM imaging of the liquid-feeding posts and vapor vents

The structure of the liquid-feeding posts and the vapor vents is revealed from SEM images. Figure 1 (b) shows a perspective view of a liquid-feeding post (d_{post} = 1 mm) fabricated by ablating away the material surrounding the post; this SEM was taken before the cap layer was attached. In the ablated region surrounding the post, the remaining sintered base wick layer remains porous, with only a slight morphology change compared to the as-sintered surface seen at the top of the post. The image in Figure 1 (b) also reveals that the laser ablation fuses a thin ring of particles around the sidewalls of the post, perpendicular to the direction of laser movement, but the native sintered wick morphology and porosity within the post is preserved. While the sides of the posts are nearly fused shut and have only a few open pores, this would not impede the primary liquid flow path through the porous core of each post. Figure 1 (c) shows a perspective view of a vapor vent (d_{vent} = 1 mm). The sidewall of the vent is fused, as in the case of the posts, while the surrounding bulk wick in the cap layer is unaffected. Despite the side walls being fused, evaporation is not required from the side surfaces of the posts or vents, and therefore, the lack of open pores on these surfaces is not expected to affect the thermal performance (and may even assist in preventing liquid entrainment into the vapor flow pathways). We have thus confirmed that the laser machining process successfully achieves the necessary features for top-down liquid feeding and vapor venting.

To check the alignment between the posts and the vents after fabrication, a quarter section was cut out from the full two-layer wick sample and imaged. To prevent abrasion damage to the sintered particles, this sectioning was achieved using the laser to cut through the entire two-layer wick thickness and solid copper substrate. Figure 1 (d) shows a perspective cutaway view of the sectioned two-layer wick. The liquid-feeding posts are seen to be present underneath the cap layer and offset from the vents. The base wick layer thickness above the substrate is also visible.

2.2 μ-CT scans of the two-layer wick

The internal structure of the evaporator wick was investigated by μ-CT scanning (Bruker Skyscan 1272) in the Center for Particulate and Powder Processing at Purdue University. A low-resolution scan (1632 × 1092 pixels; 16.4 μm voxels) was performed to check the alignment and connectivity of the posts and vents, as well as the presence of the thin base layer. Figure 2 (a) shows a schematic diagram of a plan view of the two-layer wick sample fabricated for μ-CT scanning. Figure 2 (b) shows a series of slices obtained from the reconstruction at different locations along the two-layer wick. Figure 2 (c) shows representative schematic diagrams of the two-layer wick cross section at the same locations as the slices in Figure 2 (b), to help identify the critical features in each of the scan images. Slice 1 is through the bulk wick in a region outside of the 1 cm^2 two-layer evaporator wick area. A monolithic layer of porous particles is seen, with a well-connected seam formed when sintering the cap layer onto the layer below. Slice 2 is taken though the two-layer wick at a section where there are no post or vent features. The thin base layer is sintered to the substrate underneath the cap layer, with these layers separated by an internal gap equal to the height of the liquid-feeding posts. The μ-CT scan has some artificial noise within this gap above the base layer due to the difficulty for X-rays to penetrate through the solid copper. The vapor vents and the liquid-feeding posts are visible in slices 3 and 4, respectively. There is some tapering of the post and vent sidewalls that results from the laser machining process, which is not material to their intended functioning. Importantly, the posts are seen to be well-sintered to the cap layer, providing a continuous pathway for top-down liquid feeding to the thin base layer. Overall, the μ-CT scan images reveal that the sintering and laser machining processes are successful in ensuring the connectivity of the liquid-feeding features to the base wick layer. In addition, the features of the two-layer wick are confirmed to remain intact after fabrication.

3 Capillary-fed boiling experimental characterization

3.1 Experimental facility and procedures

An experimental facility is used to study boiling heat transfer from the capillary-fed wicks under conditions that mimic the evaporator region of a vapor chamber. The evaporator wicks are tested in a saturated environment while being fed with liquid uniformly from all directions; the wick is not submerged and flooding over the top of the wick is avoided. The experimental facility is described comprehensively in Ref. [18] and is summarized in brief here.

Figure 3 shows a photograph of the assembled test facility with important parts labeled. The facility consists of a test chamber with a heater assembly attached to the bottom wall that applies a heat input to the evaporator wick under test. A Graham condenser is connected to the top wall and a copper condenser coil runs inside the chamber, both connected to coolant flow lines. Chamber measurement sensors, including thermocouples in the liquid pool and vapor space and a pressure transducer, monitor the temperature and pressure to ensure that a saturated environment is maintained. Immersion heaters in the liquid pool help with degassing and to maintain saturation conditions during testing. At the start of each test, the Graham condenser is used to vent non-condensable gas while the working fluid (DI water) inside the chamber is vigorously boiled by the cartridge heaters. After degassing, the chamber is sealed from the ambient and is maintained as a saturated environment at 100 °C by adjusting the coolant flow rate through the internal condenser coil. The fluid level in the chamber is higher than the evaporator wick, but a dam that seals against the top perimeter of the wick prevents flooding over the wick. The dam has openings to allow for the wick to uniformly draw liquid from the periphery by capillary action. The surrounding liquid pool is ~1 cm above the wick level through the duration of the boiling test; at this height, the hydrostatic pressure head is ~30 times smaller than the capillary pressure. Hence, any gravitational assistance to liquid feeding has a negligible effect on the dryout heat flux of the wick. A window in the top wall of the chamber overlooks the middle 1 cm^2 heated area of the wick to allow for visualization; visualizations are obtained with a high-speed camera (Phantom VEO 710L; Nikon Micro-Nikkor 200 mm lens).

The wick substrate is soldered to the top 10 mm × 10 mm surface of a copper heater block in an insulated heater assembly. The solder provides a low-resistance thermal connection between the heater block and the substrate. The heater block is instrumented with thermocouples to directly measure the heat flux and determine the wick substrate temperature by extrapolation. The heater block specifications, data reduction procedure, and uncertainty quantification are presented in Ref. [18]. A layer of mineral wool and PEEK insulation surround the copper heater block.

Prior to testing, the wicks are treated in a dilute piranha solution to strip the surface of any oxides and organic contaminants. The piranha solution is prepared by diluting 15 ml of 96% sulphuric acid (H_2SO_4) and 5 ml of 30% hydrogen peroxide (H_2O_2) into 100 ml (total volume) aqueous solution. The wicks are soaked in the solution for 60 sec. The copper wicks are then rinsed in DI water and dried thoroughly with a compressed nitrogen gun. The wicks are then immediately sealed into the chamber. For each wick sample, the relationship between imposed heat flux and substrate temperature (boiling curve) is established, and the thermal resistance is determined at each heat flux. Each test is carried out by increasing the heat input in steps and allowing the system to reach steady state at each heat input value. The test is terminated when dryout is reached; dryout is characterized by a sudden rise in the substrate temperature that does not settle to a steady value. In this work, the substrate superheat at the first steady heat input value was high enough to initiate nucleate boiling in the wick; capillary-fed boiling occurs in all of the steady data points reported.

3.2 Single-layer wicks testing: effect of sintered particle size

A reduced-order model of the thermal-fluid performance of the two-layer wick, developed in our previous work [17], revealed that the maximum pressure drop occurs in the base wick layer, because of the small cross-sectional area available for fluid flow. Therefore, any change in the particle formulation of this thin porous base wick layer may result in significant changes in performance of the two-layer wick. We evaluate the effect of sintered particle size on capillary-fed boiling by fabricating three different single-layer wicks. Figure 4 shows plan and section views of the single-layer wick design. The wick has a thin, uniform layer of sintered particles over the central 1 cm^2 evaporator area; the thickness, t_{base}, is identical to the base layer thickness of the two-layer wick. This thin layer is supplied with liquid from the periphery by a thicker bulk wick (thickness t_{bulk}).

The wicks are fabricated by sintering a wick of thickness t_{bulk} over a square area with edge length l_{bulk}, followed by laser machining the middle 1 cm^2 region down to a thickness, t_{base}. Details of the three wicks tested are given in Table 2, fabricated from three different particle size ranges: 45-53 μm, 90-106 μm and 180-212 μm. Each single-layer wick in the table is denoted by a sample ID, which contains the particle size range followed by the thickness (t_{base}) of the evaporator region. The 90-106 μm and 180-212 μm single-layer wicks have two particle diameters across their thickness, while the 45-53 μm wick has four particle diameters across its thickness. Figure 5 shows SEM images of the sintered wicks for each different particle size range. The two smaller particle size ranges have irregular-shaped particles manufactured by water atomization, while the larger 180-212 μm particles contain a mix of spherical and irregular particle geometries. Table 2 also lists the porosity and a calculated value of permeability for the samples. The porosity is calculated by measuring the weight and volume of the sintered porous layer after sintering. The Carman-Kozeny equation ($K = D^2\varphi^3/(1-\varphi)^2$) is used to estimate the permeability, where D is the mean particle size and φ is the porosity of the wick.

Figure 6 (a) and (b) respectively show the boiling curve and wick thermal resistance for the three single-layer wicks. Each boiling curve is characterized by an initial near-linear slope, indicative of a constant thermal resistance and uniform capillary-fed boiling over the entire heat input area. For the two samples with smaller particle sizes, 45-53:200 and 90-106:400, at some heat flux, there is a reduction in slope of the boiling curve and increase in thermal resistance associated with partial dryout in the center of the wick. The trends in the thermal resistance before partial dryout, as well as the heat flux at which partial dryout occurs, are both monotonic with particle size. The wick with the smallest particle sizes, 45-53:200, has the highest resistance that is constant at ~0.27 K/W till dryout begins at ~ 54 W/cm^2, above which the thermal resistance increases with heat flux; complete dryout occurs at 115 W/cm^2. Wick 90-106:400 exhibits a lower constant thermal resistance of ~ 0.15 K/W up to 122 W/cm^2, after which partial dryout begins; complete dryout occurs at 175 W/cm^2. In contrast, partial dryout is not observed in wick 180-212:400 and the resistance is nearly constant (decreases slightly with increasing heat flux) throughout the test. After the last steady data point at 193 W/cm^2, at a wick resistance of 0.075 K/W, complete dryout is triggered.

The trend in wick resistance with particle size, over the range of heat fluxes before partial dryout, can be attributed to the impedance to vapor removal from the wick during boiling. Considering the low permeability of the smaller 45-53 μm particles, vapor escaping the wick incurs a large pressure drop as it flows up through the pore paths. Any pressure drop in the vapor corresponds to an increased saturation temperature drop across the wick thickness. Sample 180-212:400 has the highest permeability and therefore imposes the lowest hydraulic, and hence thermal, resistance. The increase in thermal resistance after the onset of partial dryout in each case is trivially explained from the visualizations; during the partial dryout regime, the center of the heated area is devoid of all liquid and capillary-fed boiling cannot occur in this region, resulting in an increased thermal resistance.

The effect of particle size in sintered coatings on pool boiling behavior has been extensively studied in the literature [19,20]. In addition, there have been detailed characterizations and statistical descriptions of sintered wick structures [21], and their effects on pool boiling [22]. However, few studies have addressed the effect of particle size during capillary-fed boiling; moreover, the wick types, heating area, and wick thicknesses differ between each of these studies. Weibel *et al.* [14] tested the thermal resistance of ~1 mm-thick sintered wicks with three different particle sizes and observed a minimum thermal resistance at an intermediate optimum particle size. Investigations on monolayer sintered porous wicks with different particle sizes performed by Ju *et al.* [7] revealed a higher wick resistance for lower particle sizes. Li *et al.* [23] considered sintered screen mesh wicks and reported that the dryout limit was higher for wicks with larger pore sizes. This was attributed to the decreased flow resistance to capillary flow if the wicks possessed larger pore sizes. In the present work, wick 180-212:400 gave the best boiling performance, providing the highest complete dryout limit along with a low value of thermal resistance. This is attributed to the high permeability of the wick, which allows for ease of liquid feeding. Although the capillary pressure is lower for larger particle sizes ($P_c \sim 1/D$), the effect of the larger wick permeability ($K \sim D^2$), outweighs the effect of the reduced capillary pressure for this evaporator design.

3.3 Two-layer wick testing

A two-layer evaporator wick was fabricated with the 180-212 μm particle size range that provided the highest dryout heat flux among the single-layer wicks. It was shown in our previous work [17,18] that denser liquid-feeding post arrays provided a significant improvement in the dryout heat flux without a penalty in the wick resistance. Following this design rule, a two-layer wick with a 15 × 15 array of posts is fabricated to demonstrate high-heat-flux dissipation. Figure 7 shows a plan and sectioned side view of the two-layer wick design (identified as 180-212:15×15). The two-layer region is fabricated over a larger 15 mm × 15 mm area (denoted by $l_{two\text{-}layer}$ = 15 mm), while the heat input is the same 10 mm × 10 mm area in the center of the wick (denoted by l_{evap} = 10 mm). This larger two-layer region was used to take advantage of heat spreading in the substrate underneath the wick. A 3D conduction simulation was performed to select the larger two-layer wick region. This heat spreading analysis assumed a uniform heat flux over a 10 mm × 10 mm region on the underside of the substrate, and a uniform heat transfer coefficient on the top side (treating all other boundaries as insulated). The values of the heat transfer coefficient as a function of heat flux were specified based on our prior experiments for capillary-fed boiling in two-layer wicks [18]. A 15 mm × 15 mm region was identified as the optimal size for the two-layer wick region; further increases in this area would not further reduce the effective total thermal resistance via heat spreading, but would unfavorably increase the length over which capillary feeding would need to occur within the two-layer wick (likely reducing the maximum heat flux that could be dissipated). Appendix A includes the analysis performed to calculate the heat spreading area, and the effect of heat spreading on the total thermal resistance of the two-layer wick. In the facility, the dam that seals this wick has an enlarged 15 mm × 15 mm opening to allow unrestricted release of vapor. The important dimensions of the wick are as follows:

d_{post} = 650 μm, d_{vent} = 500 μm, t_{post} = 400 μm, t_{cap} = 700 μm, and t_{base} = 400 μm (see Figure 7 for symbol definitions). The base wick thickness and particle composition are the same as in the 180-212:400 single-layer wick.

Figure 8 shows the boiling curve and the wick resistance for the two-layer wick (180-212:15×15). In Figure 8 (a), the two-layer wick shows a near-linear increase in wick superheat as the heat flux increases till ~130 W/cm^2, after which a change in slope is observed. At low heat fluxes, only the center heated area (10 mm × 10 mm) boils; once the heat flux exceeds ~130 W/cm^2, a larger area undergoes boiling, causing a reduction in the measured thermal resistance thereafter. Above a heat flux of ~240 W/cm^2, the two-layer wick maintains a near constant resistance; as explained in Ref. [18], once the heat flux exceeds this value, the liquid recedes from the empty spaces between the posts in the wick into the cap layer and within the posts, providing separated pathways for liquid and vapor flow. In this desired mode of operation, the post and cap layers do not impose any additional thermal resistance. Ultimately, the two-layer wick achieves a dryout limit of 485 W/cm^2 at a low thermal resistance of 0.052 K/W. Sudden dryout is triggered beyond 485 W/cm^2 when the menisci in the liquid-feeding cap layer recede completely. It can be noted that partial dryout is not seen in the two-layer wick due to the uniform liquid supply over the entire heated area from the cap layer.

The supporting information (Appendix B) provides high-speed videos of the phase change process in the two-layer wick, captured at different steady heat fluxes along the boiling curve. The boiling behavior in the two-layer wick is characterized by bubbling through the vents at low heat fluxes, followed by a transition to vapor jetting out of the vents at high heat fluxes. During the boiling process, it was observed that high-speed vapor flow out of the vents entrains liquid droplets that spray out of the wick, potentially reducing the total mass of liquid being effectively fed to the evaporator region. This is similar to the results observed by Cai and Chen [11], who reported up to 12% liquid loss due to spraying from their biporous wick, which directly affected the dryout limit. In the two-layer wick, some of the liquid spray from the boiling layer (base wick) is expected to be captured by the cap layer above, thereby reducing the total liquid loss compared to single-layer wicks.

4 Discussion

The two-layer wick provides a combination of high-heat-flux dissipation from large heated areas along with a low thermal resistance. In this section, the thermal test results from the two-layer wick in this work are compared against various prior investigations reported in the literature on capillary-fed boiling in porous wicks. Figure 9 (a) shows a plot of the maximum heat flux dissipated as a function of heated area, from among the references listed in Table 1. This plot reinforces the inverse relationship between heater size and the dryout heat flux described in the introduction. Extremely high heat fluxes of ~700 W/cm^2 and higher have only been dissipated over very small hotspots of less than 10 mm^2. For example, the highest reported heat flux of ~1250 W/cm^2 [24] was attained over a very small hotspot of 0.6 mm^2. As the heater sizes increase, the dryout heat fluxes are reduced. Cai and Bhunia [25] noted a decrease in dryout heat flux for carbon nanotube biporous wicks from 770 to 140 W/cm^2 for an increase in heater area from 4 mm^2 to 100 mm^2. Similarly, Nam *et al.* [15] reported that the dryout limit of nanostructured micro-post wicks decreased from ~800 W/cm^2 to 200 W/cm^2 when the heater size was increased from 4 mm^2 to 25 mm^2. In the case of a small hotspot (as opposed to a larger heating area), the liquid must be fed only over a small area of wick to avoid dryout. This reduced flow length significantly reduces the pressure drop in the wick. In addition, for a small hotspot, heat spreading in the underlying substrate plays a stronger role in effectively increasing the area available for phase change. For these reasons, the dryout limits are always lower for larger heater sizes. Consequently, there are only two reports of ~500 W/cm^2 heat dissipation over a relatively large, 1 cm^2 area. Hwang *et al.* [6] developed a sintered evaporator wick with lateral feeding arteries that supply liquid to a thin monolayer of sintered particles. They reported a maximum heat flux dissipation of 580 W/cm^2 over 1 cm^2, albeit at a high surface superheat temperature of 72 K due to the occurrence of partial dryout. The two-layer wick reported here provides a maximum heat flux dissipation of 485 W/cm^2 (star symbol in Figure 9 (a)) over 1 cm^2 heat input area, at a significantly lower superheat of only 25 K due to avoidance of partial dryout by the top-down liquid feeding approach.

A new capillary-fed boiling performance map is developed and shown in Figure 9 (b) to identify wick types that can simultaneously provide *high power* and *low thermal resistance* operation. This figure plots the thermal resistance at the maximum power level against the maximum total power dissipated. Data points in the region of the plot towards the bottom right indicate superior performance. Although various studies have shown high-heat-flux values, the total power dissipated has been low, owing to the smaller heater areas. In general, thick wicks with multiple layers of sintered particles can dissipate high powers but exhibit large thermal resistances, due to vapor clogging in the pore spaces of the wick during boiling [10]. Reductions in thermal resistance are achieved by providing separate, high-permeability pathways for vapor flow out of the wick, such as with grooved channels [8], grid-patterns [26] or high-permeability foams [9]. In comparison to all previous wicks tested in the literature, the two-layer wick (star symbol in Figure 9 (b)) achieves a unique combination of high power dissipation (485 ± 27 W) combined with a low thermal resistance (0.052 ± 0.008 K/W).

5 Conclusions

This study demonstrated high-heat-flux passive dissipation using capillary-fed boiling in a two-layer sintered evaporator wick. The two-layer wick concept uses a thin base-wick layer combined with additional dedicated liquid-feeding and vapor-removal structures to separate the liquid feeding and vapor removal pathways in the porous wick during boiling. The two-layer wick was fabricated using a combination of sintering and laser machining process steps; SEM images and μ-CT scans were analyzed to characterize the as-fabricated internal structures of the two-layer wick. Three single-layer wicks having different particle sizes were fabricated and tested to determine the optimal size range given the strong influence of wick formulation on capillary-fed boiling performance. Increasing the particle size led to an increase in the dryout limit as well as a decrease in the thermal resistance during capillary-fed boiling. This was attributed to an increased permeability provided by larger particle sizes that offered a reduction in the flow impedance to both liquid feeding and vapor removal. To realize high-heat-flux dissipation, a two-layer wick with a 15 × 15 array of liquid-feeding posts was sintered using the largest (180-212 μm) particles. This two-layer wick dissipated a maximum of 485 W/cm^2 over 1 cm^2 at a thermal resistance of 0.052 K/W. Comparing this thermal performance to prior work reported in the literature on capillary-fed boiling reveals that the two-layer wick is able to provide an unprecedented combination of high total power heat dissipation at low thermal resistance.

Acknowledgements

This material is based upon work supported by Toyota Motor Engineering and Manufacturing North America, Inc., under an Advanced Research Collaboration between Purdue University and the Toyota Research Institute of North America.

Appendix A

Supplementary material for the heat spreading analysis can be found online.

Appendix B

Supplementary high-speed videos associated with the article can be found online.

List of Tables

List of Figures

Figure 1. (a) Schematic diagram of a two-layer evaporator wick with a 4 × 4 array of liquid-feeding posts and an offset 3 × 3 array of vapor vents. The primary flow pathways for liquid (in blue) and vapor (in red) are indicated. SEM images are taken during the fabrication of the wick to show the structure of (b) a liquid-feeding post before the cap layer is attached and (c) a vapor vent in the cap layer. (d) An SEM image of a cutaway view of the sectioned two-layer wick sample.

Figure 2. (a) Plan view of the two-layer evaporator wick sample (4 × 4 posts, 3 × 3 vents) used for μ-CT scan imaging. (b) Reconstructed side-view slices from a μ-CT scan of the evaporator wick at different vertical cross-sections across the wick. (c) Schematic diagrams illustrating the different wick features identified in the scan images.

Figure 3. A side-view photograph of the experimental test facility with important parts labeled.

Figure 4. Plan and section view diagrams of the single-layer wick design. The single-layer wick has a thickness t_{base} over the central evaporator area, supplied by a thicker bulk wick of thickness t_{bulk}.

Figure 5. SEM images of sintered wicks with different particle size ranges of (a) 45 – 53 μm, (b) 90 – 106 μm, and (c) 180 – 212 μm.

Figure 6. (a) Capillary-fed boiling curves and (b) wick resistance versus heat fluxes for the three single-layer wick designs, each sintered with a different particle size range. The error bars represent the uncertainty in the measured heat flux and the wick resistance. The legend nomenclature indicates the particle size range and the wick thickness in microns.

Figure 7. Schematic diagram (plan and side view) of the two-layer evaporator wick tested in this work. This design consists of a 15 × 15 array of vertical liquid feeding posts and an offset 14 × 14 array of vapor vents over a 1.5 cm × 1.5 cm area. The evaporator region is the center 1 cm^2 area (d_{post} = 650 μm; d_{vent} = 500 μm; t_{post} = 400 μm; t_{cap} = 700 μm; t_{base} = 400 μm).

Figure 8. (a) Boiling curves and (b) wick resistance for the two-layer wick comprised of 180-212 μm particles. The two-layer wick has a 15 × 15 array of liquid-feeding posts over a 15 mm × 15 mm area.

Figure 9. Compilation of capillary-fed boiling performance of different evaporator wicks tested in the literature: (a) Maximum heat flux versus heater area and (b) maximum power versus resistance at the corresponding power (values above 0.2 K/W are omitted to focus on the low-resistance data; all omitted data fall below a maximum power of 200 W). In comparison to other evaporator wicks, the two-layer wick (star symbol) *achieves high-heat-flux dissipation over a large heater area (i.e., higher power) at a lower thermal resistance*.

Table 1. Recent developments in capillary-fed evaporation/boiling on evaporator wicks for high-heat-flux dissipation. All of the studies included use water as the working fluid. The superheat and thermal resistance correspond to the values as measured at the maximum heat flux/power.

Reference		**Evaporator Wick Type**	**Saturation Temp. (°C)**	**Heater Size[*] (mm^2)**	**Maximum Heat Flux (W/cm^2)**	**Maximum Power (W)**	**Superheat (K)**	**Thermal Resistance (K/W)**
Semenic and Catton [10]	2009	Biporous sintered copper particles	40	32 (circular)	990	317	147	0.46
Weibel *et al.* [14]	2010	Sintered copper particles	100	25	596	149	26	0.17
Hwang *et al.* [6]	2011	Lateral converging arteries supplying a monolayer of sintered copper particles	43	100	580	580	72	0.12
Nam *et al.* [15]	2011	Nanostructured copper microposts	44	25	160	40.0	32	0.80
				4	800	32.0	35	1.1
Cai and Chen [11]	2011	Biporous carbon nanotube pillars	100	100	190	190	90	0.47
				4	938	37.5	94	2.5
Weibel *et al.* [26]	2012	Grid-patterned sintered copper particles	100	25	580	145	17	0.12
Coso and Srinivasan [12]	2012	Biporous silicon pin fins	100	100	277	277	14	0.051
				6.25	733	45.8	7	0.15
Cai and Bhunia [25]	2012	Biporous carbon nanotube pillars/stripes	100	4	770	30.8	35	1.1
				100	140	140	25	0.18
Dai *et al.* [8]	2013	Copper screen mesh sintered on microchannels	100	100	153	153	17	0.11
Palko *et al.* [24]	2015	Copper inverse opals	100	0.6 (0.3 mm × 2 mm)	1250	7.5	10	1.3
Ryu *et al.* [9]	2017	Copper metal foam supplying a copper micro-post layer	30	16	429	68.6	79	1.2
Lv and Li [27]	2017	Sintered copper mesh	-	10 (5 mm × 2 mm)	490	49	-	1.1
This work		Two-layer sintered copper particles	100	100	485	485	25	0.052

*All heaters are square unless otherwise noted

Table 2. Properties of the single-layer sintered porous wicks.

Sample ID	**Particle sizes (μm)**	**Thickness, t_{base} (μm)**	**Measured porosity, φ**	**Calculated permeability, K (m^2)**
45-53:200	45-53	200	0.61	3.730×10^{-9}
90-106:400	90-106	400	0.61	1.433×10^{-8}
180-212:400	180-212	400	0.63	6.334×10^{-8}

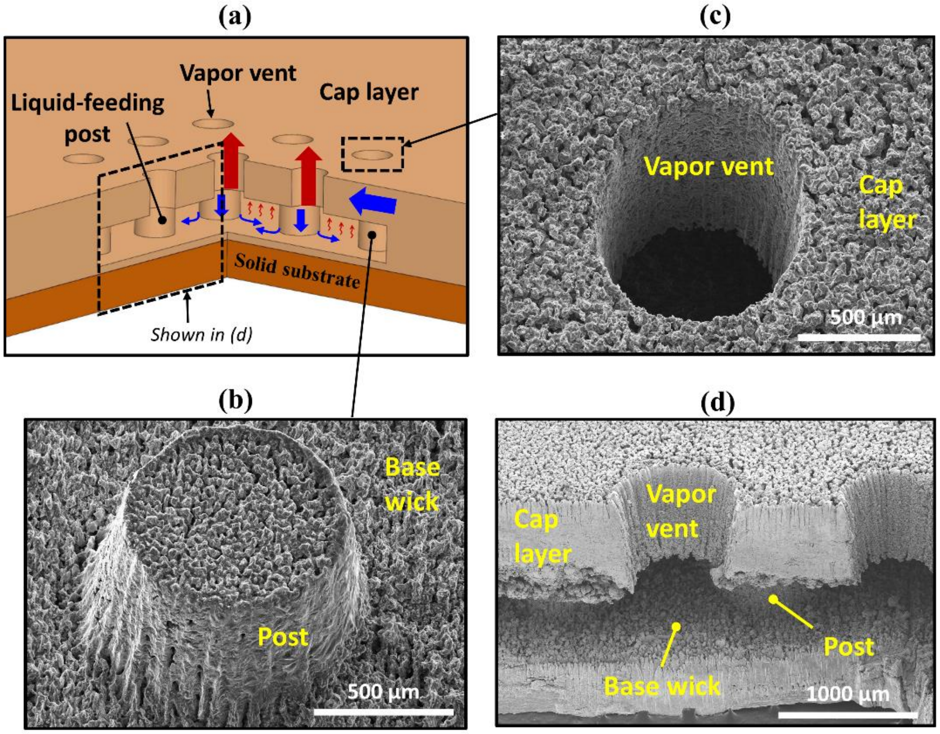

Figure 1. (a) Schematic diagram of a two-layer evaporator wick with a 4 × 4 array of liquid-feeding posts and an offset 3 × 3 array of vapor vents. The primary flow pathways for liquid (in blue) and vapor (in red) are indicated. SEM images are taken during the fabrication of the wick to show the structure of (b) a liquid-feeding post before the cap layer is attached and (c) a vapor vent in the cap layer. (d) An SEM image of a cutaway view of the sectioned two-layer wick sample.

(note for editor: 1.5 columns wide)

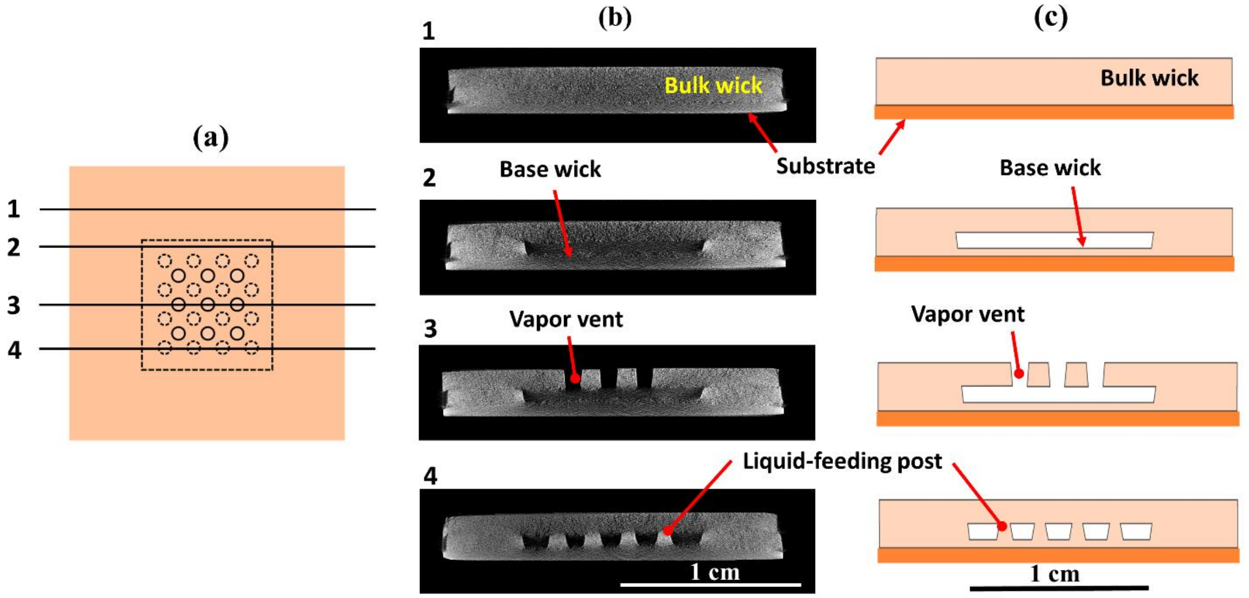

Figure 2. (a) Plan view of the two-layer evaporator wick sample (4 × 4 posts, 3 × 3 vents) used for μ-CT scan imaging. (b) Reconstructed side-view slices from a μ-CT scan of the evaporator wick at different vertical cross-sections across the wick. (c) Schematic diagrams illustrating the different wick features identified in the scan images.

(note for editor: 2 columns wide)

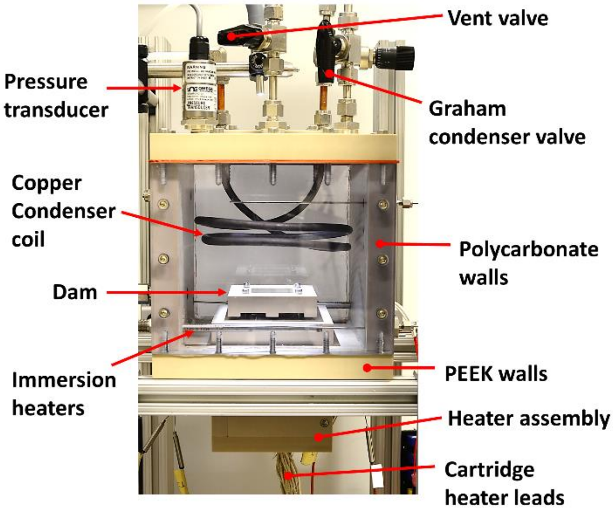

Figure 3. A side-view photograph of the experimental test facility with important parts labeled.

(note for editor: 1 column wide)

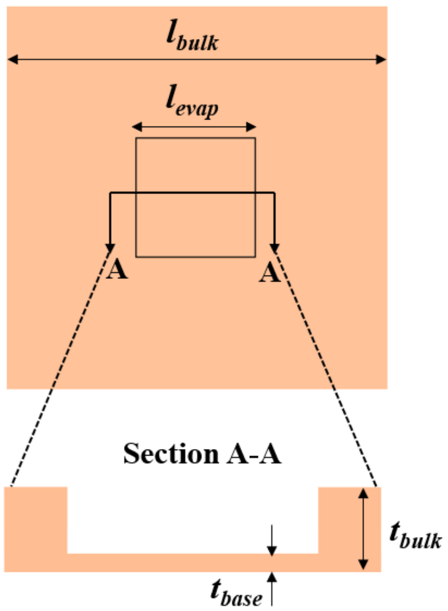

Figure 4. Plan and section view diagrams of the single-layer wick design. The single-layer wick has a thickness t_{base} over the central evaporator area, supplied by a thicker bulk wick of thickness t_{bulk}.

(note for editor: 1 column wide)

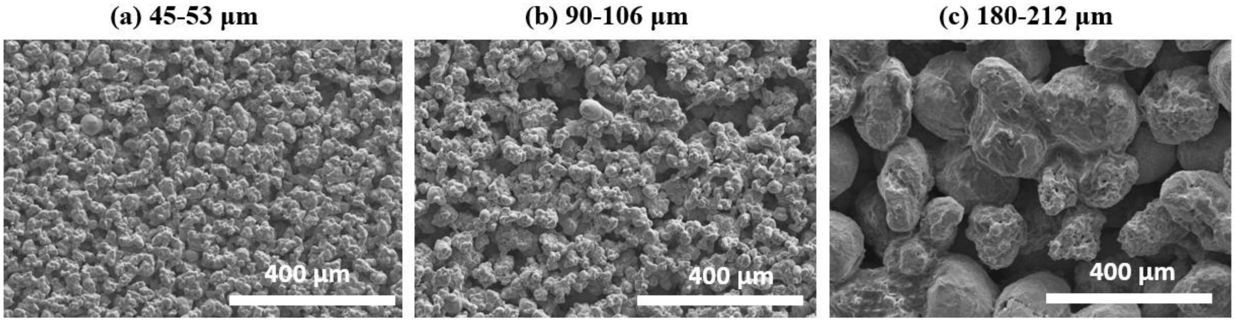

Figure 5. SEM images of sintered wicks with different particle size ranges of (a) 45 – 53 µm, (b) 90 – 106 µm, and (c) 180 – 212 µm.

(note for editor: 2 columns wide)

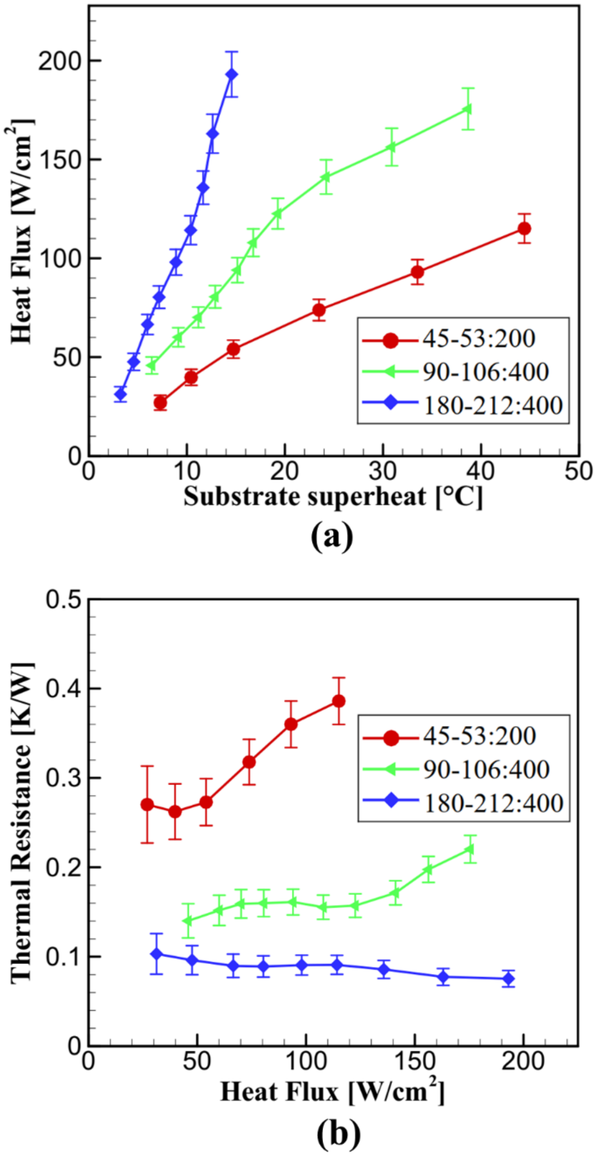

Figure 6. (a) Capillary-fed boiling curves and (b) wick resistance versus heat fluxes for the three single-layer wick designs, each sintered with a different particle size range. The error bars represent the uncertainty in the measured heat flux and the wick resistance. The legend nomenclature indicates the particle size range and the wick thickness in microns.

(note for editor: 1 column wide)

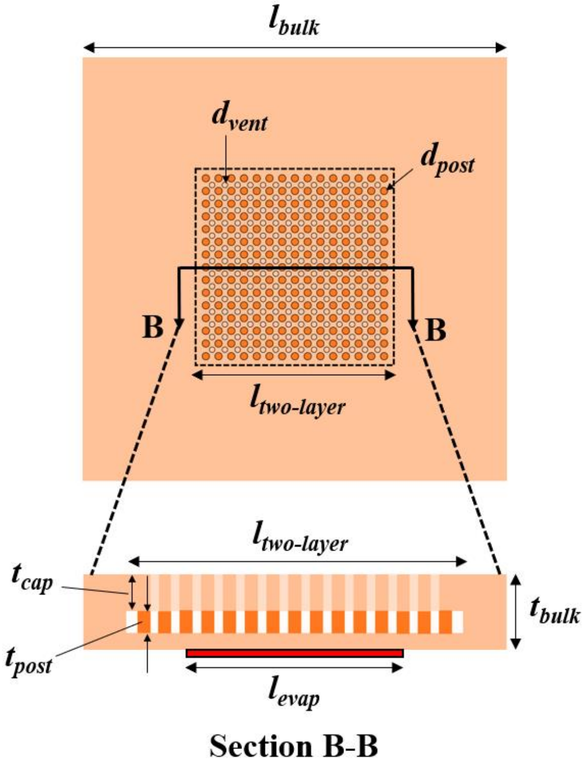

Figure 7. Schematic diagram (plan and side view) of the two-layer evaporator wick tested in this work. This design consists of a 15 × 15 array of vertical liquid feeding posts and an offset 14 × 14 array of vapor vents over a 15 mm × 15 mm area. In the plan view, the open circles are the vents and the filled circles represent the posts below. The evaporator region is the center 10 mm × 10 mm area (d_{post} = 650 µm; d_{vent} = 500 µm; t_{post} = 400 µm; t_{cap} = 700 µm; t_{base} = 400 µm).

(note for editor: 1 column wide)

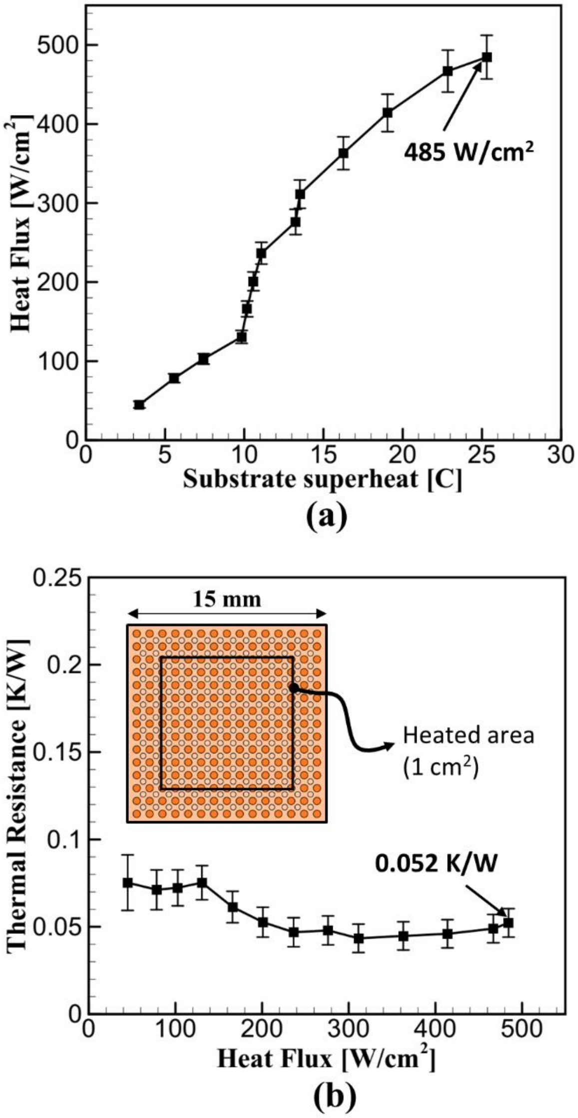

Figure 8. (a) Boiling curves and (b) wick resistance for the two-layer wick comprised of 180-212 μm particles. The two-layer wick has a 15 × 15 array of liquid-feeding posts over a 15 mm × 15 mm area.

(note for editor: 1 column wide)

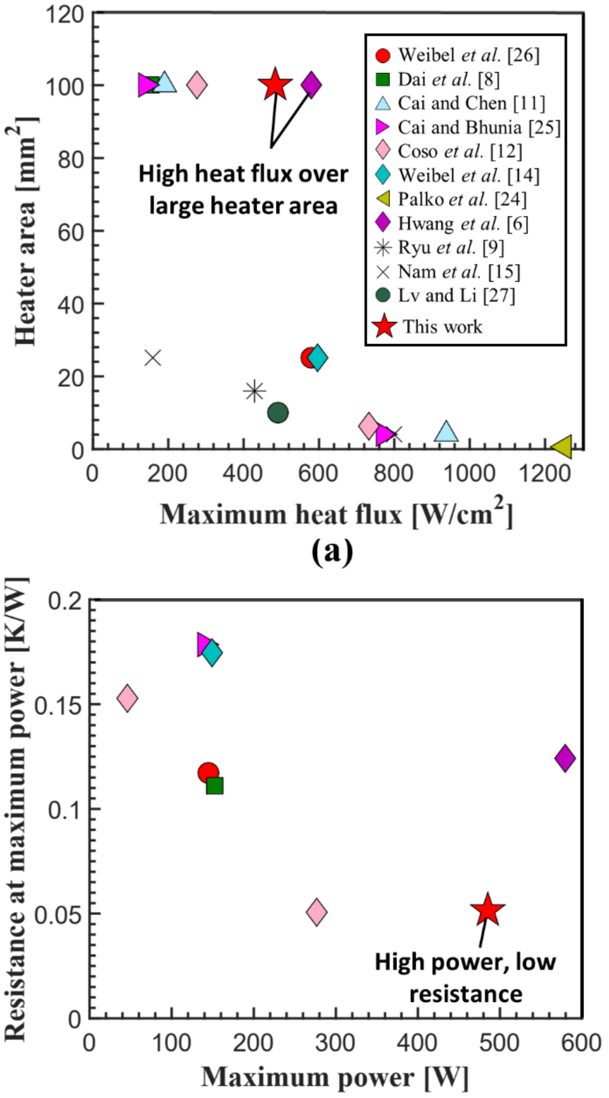

(a)

(b)

Figure 9. Compilation of capillary-fed boiling performance of different evaporator wicks tested in the literature: (a) Maximum heat flux as a function of heater area and (b) resistance at maximum power as a function of the corresponding power (values above 0.2 K/W are omitted to focus on the low-resistance data; all omitted data fall below a maximum power of 200 W). In comparison to other evaporator wicks, the two-layer wick (star symbol) *achieves high-heat-flux dissipation over a large heater area (i.e., higher power) at a lower thermal resistance*.

(note for editor: 1 column wide)

References

[1] A. Faghri, “Review and advances in heat pipe science and technology,” *J. Heat Transfer*, vol. 134, pp. 123001–18, 2012.

[2] H. N. Chaudhry, B. R. Hughes, and S. A. Ghani, “A review of heat pipe systems for heat recovery and renewable energy applications,” *Renewable and Sustainable Energy Reviews*, vol. 16, pp. 2249–2259, 2012.

[3] H. Tang, Y. Tang, Z. Wan, J. Li, W. Yuan, L. Lu, Y. Li and K. Tang, “Review of applications and developments of ultra-thin micro heat pipes for electronic cooling,” *Applied Energy*, vol. 223, pp. 383–400, 2018.

[4] A. Bar-Cohen, K. Matin, N. Jankowski, and D. Sharar, “Two-Phase Thermal Ground Planes: technology development and parametric results,” *J. Electron. Packag*, vol. 137, pp. 010801–9, 2014.

[5] J. A. Weibel and S. V. Garimella, “Chapter Four - Recent advances in vapor chamber transport characterization for high-heat-flux applications,” in *Advances in Heat Transfer*, vol. 45, Elsevier, pp. 209–301, 2013.

[6] G. S. Hwang, E. Fleming, B. Carne, S. Sharratt, Y. Nam, P. Dussinger, Y. S. Ju and M. Kaviany, “Multi-artery heat-pipe spreader: Lateral liquid supply,” *International Journal of Heat and Mass Transfer*, vol. 54, pp. 2334–2340, 2011.

[7] Y. S. Ju, M. Kaviany, Y. Nam, S. Sharratt, G. S. Hwang, I. Catton, E. Fleming and P. Dussinger, “Planar vapor chamber with hybrid evaporator wicks for the thermal management of high-heat-flux and high-power optoelectronic devices,” *International Journal of Heat and Mass Transfer*, vol. 60, pp. 163–169, 2013.

[8] X. Dai, F. Yang, R. Yang, Y.-C. Lee, and C. Li, “Micromembrane-enhanced capillary evaporation,” *International Journal of Heat and Mass Transfer*, vol. 64, pp. 1101–1108, 2013.

[9] S. Ryu, J. Han, J. Kim, C. Lee, and Y. Nam, “Enhanced heat transfer using metal foam liquid supply layers for micro heat spreaders,” *International Journal of Heat and Mass Transfer*, vol. 108, Part B, pp. 2338–2345, 2017.

[10] T. Semenic, Y. Y. Lin, I. Catton, and D. B. Sarraf, “Use of biporous wicks to remove high heat fluxes,” *Applied Thermal Engineering*, vol. 28, pp. 278–283, 2008.

[11] Q. Cai and Y.-C. Chen, “Investigations of biporous wick structure dryout,” *J. Heat Transfer*, vol. 134, p. 021503, 2011.

[12] D. Ćoso, V. Srinivasan, M.-C. Lu, J.-Y. Chang, and A. Majumdar, “Enhanced heat transfer in biporous wicks in the thin liquid film evaporation and boiling regimes,” *J. Heat Transfer*, vol. 134, p. 101501, 2012.

[13] C. Byon and S. J. Kim, “Effects of geometrical parameters on the boiling limit of bi-porous wicks,” *International Journal of Heat and Mass Transfer*, vol. 55, pp. 7884–7891, 2012.

[14] J. A. Weibel, S. V. Garimella, and M. T. North, "Characterization of evaporation and boiling from sintered powder wicks fed by capillary action," *International Journal of Heat and Mass Transfer*, vol. 53, pp. 4204–4215, 2010.

[15] Y. Nam, S. Sharratt, G. Cha, and Y. S. Ju, "Characterization and modeling of the heat transfer performance of nanostructured Cu micropost wicks," *J. Heat Transfer*, vol. 133, p. 101502, 2011.

[16] P. Xu and Q. Li, "Visualization study on the enhancement of heat transfer for the groove flat-plate heat pipe with nanoflower coated CuO layer," *Appl. Phys. Lett.*, vol. 111, p. 141609, 2017.

[17] S. Sudhakar, J. A. Weibel, and S. V. Garimella, "Design of an Area-Scalable Two-Layer Evaporator Wick for High-Heat-Flux Vapor Chambers," *IEEE Transactions on Components, Packaging and Manufacturing Technology, early access*, doi: 10.1109/TCPMT.2018.2860961.

[18] S. Sudhakar, J. A. Weibel, and S. V. Garimella, "Experimental investigation of boiling regimes in a capillary-fed two-layer evaporator wick," *International Journal of Heat and Mass Transfer*, submitted for publication.

[19] C. Li and G. P. Peterson, "Parametric study of pool boiling on horizontal highly conductive microporous coated surfaces," *J. Heat Transfer*, vol. 129, pp. 1465–1475, 2007.

[20] S. Sarangi, J. A. Weibel, and S. V. Garimella, "Effect of particle size on surface-coating enhancement of pool boiling heat transfer," *International Journal of Heat and Mass Transfer*, vol. 81, pp. 103–113, 2015.

[21] K. K. Bodla, J. Y. Murthy, and S. V. Garimella, "Direct simulation of thermal transport through sintered wick microstructures," *Journal of heat transfer*, vol. 134, no. 1, p. 012602, 2012.

[22] S. Sarangi, J. A. Weibel, and S. V. Garimella, "Quantitative Evaluation of the Dependence of Pool Boiling Heat Transfer Enhancement on Sintered Particle Coating Characteristics," *Journal of Heat Transfer*, vol. 139, no. 2, pp. 021502–13, 2016.

[23] C. Li and G. P. Peterson, "Evaporation/Boiling in thin capillary wicks (II)—Effects of volumetric porosity and mesh size," *J. Heat Transfer*, vol. 128, pp. 1320–1328, 2006.

[24] J. W. Palko, C. Zhang, J. D. Wilbur, T. J. Dusseault, M. Asheghi, K. E. Goodson and J. G. Santiago, "Approaching the limits of two-phase boiling heat transfer: High heat flux and low superheat," *Applied Physics Letters*, vol. 107, p. 253903, 2015.

[25] Q. Cai and A. Bhunia, "High heat flux phase change on porous carbon nanotube structures," *International Journal of Heat and Mass Transfer*, vol. 55, pp. 5544–5551, 2012.

[26] J. A. Weibel and S. V. Garimella, "Visualization of vapor formation regimes during capillary-fed boiling in sintered-powder heat pipe wicks," *International Journal of Heat and Mass Transfer* 55, pp. 3498–3510, 2012.

[27] L. Lv and J. Li, "Managing high heat flux up to 500 W/cm^2 through an ultra-thin flat heat pipe with superhydrophilic wick," *Applied Thermal Engineering*, vol. 122, pp. 593-600, 2017.